

Binder-Free Self-Standing Hard Carbon Electrodes Graphite-Coated by PE-CVD to Boost the Efficiency of Na-Ion Batteries

Tien-Nguyen-Khoi Trinh, Adrian Beda, Octavian-Gabriel Simionescu, Oana Brîncoveanu, Loic Vidal, and Camélia Matei Ghimbeu*

This work explores the use of plasma-enhanced chemical vapor deposition (PE-CVD) to deposit a C-coating on binder-free, self-standing electrodes (SSEs). The C-coating consists of a nanocrystalline graphite thin film with crystalline domains measuring ≈ 14 nm. Regardless of the fabrication pyrolysis temperature of SSE, an increase in crystallite size and a reduction in interlayer space and defects is observed after C-coating and post-treatment at 1500°C . Pyrolysis of the SSE at 900°C induces better coverage with the nanographitic layer during PE-CVD, but prevents the development of closed pores during post-treatment at 1500°C . In contrast, a large number of closed pores form when

the SSE is pyrolyzed at 1500°C . However, no difference in performance is observed between the C-coated SSE pyrolyzed at 900 and 1500°C and post-annealed at 1500°C , therefore, lower temperature can be advantageously used for the pyrolysis step. Nevertheless, post-treatment at 1500°C is necessary to enhance performance. For both materials, the graphite coating minimized the undesirable reactions with the electrolyte, leading to more stable and conductive solid electrolyte interphase, which improves iCE (from 91.0% to 92.5%). A high reversible capacity of 320 mAh g^{-1} is also obtained, and the higher coating's conductivity is beneficial for rate capability.

1. Introduction

Energy storage is receiving more and more attention these days, with many solutions being proposed and significant progress being made. Although sodium (Na) has been considered as an alternative to lithium (Li) in Li-ion batteries (LIBs), the intense interest and research carried out on Na-ion batteries (NIBs) make this technology a viable solution for energy storage nowadays. In particular, NIBs are increasingly recognized as a reliable solution for large-scale energy storage and grid applications.^[1,2] Na-based

technology has several advantages, mainly relating to two major aspects: 1) cost benefits, due to worldwide abundance of sodium and its low price, the use of lower cost aluminum (Al) current collectors instead of copper (Cu) in LIBs, as well as the availability of hard carbon (HC) anodes and cobalt- and nickel-free cathodes, and 2) improved security, as NIBs can be discharged and stored at low potentials.^[3–5]

The selection and optimization of anode materials are essential to develop high-performance Na-storage systems, particularly to ensure high initial Coulombic efficiency (iCE), reversible capacity, and long lifespan. Numerous studies have revealed that HC is a material with enormous potential for Na-ion storage due to its advantages, including low price, high availability, large diversity, sustainability, and high performance.^[6–8] The microstructure of HC is very complex, combining graphitic and disordered domains, surface functionalities, defects, and a particular texture consisting of open and closed pores. All these properties make this material an ideal candidate to accommodate Na ions, as highlighted by its high reversible capacity ($>300 \text{ mAh g}^{-1}$, in Nahalf-cells), which sometimes approaches the theoretical capacity of graphite in LIBs (i.e., 372 mAh g^{-1}).^[9,10]

However, some drawbacks remain, demanding new solutions and the development of advanced HC materials. Among them, the relatively low iCE, $<85\%$ for most materials,^[10–13] limits the energy density and requires excess sodium in the cathode to compensate for the initial capacity loss. The HC specific surface area (SSA) and surface chemistry, which is rich in oxygen functional groups, defects, or impurities, are important contributors to this problem,^[14–17] as they promote excessive electrolyte degradation and solid electrolyte interphase (SEI) formation.

T.-N. K. Trinh, A. Beda, L. Vidal, C. Matei Ghimbeu
Université de Haute-Alsace, Institut de Science des Matériaux de Mulhouse (IS2M), CNRS UMR 7361

15 Rue Jean Starcky, 68100 Mulhouse, France
E-mail: camelia.ghimbeu@uha.fr

T.-N. K. Trinh, A. Beda, L. Vidal, C. Matei Ghimbeu
Université de Strasbourg
67081 Strasbourg, France

T.-N. K. Trinh, A. Beda, C. Matei Ghimbeu
Réseau sur le Stockage Electrochimique de l'Energie (RS2E), CNRS FR3459
33 Rue Saint Leu, 80039 Amiens Cedex, France

O.-G. Simionescu, O. Brîncoveanu
National Institute for Research and Development in
Microtechnologies – IMT Bucharest
126A Erou Iancu Nicolae Street, 077190 Voluntari, Romania

 Supporting information for this article is available on the WWW under <https://doi.org/10.1002/batt.202500492>

 © 2025 The Author(s). *Batteries & Supercaps* published by Wiley-VCH GmbH. This is an open access article under the terms of the Creative Commons Attribution-NonCommercial-NoDerivs License, which permits use and distribution in any medium, provided the original work is properly cited, the use is non-commercial and no modifications or adaptations are made.

Therefore, the irregular microstructure of HC along with the thick (inhomogeneous) passivation layer lower the lifespan of HC in NIBs compared to graphite in LIBs.

The diversity of HC precursors and synthesis pathways allows HC materials to be prepared mainly in powder form, but also in monolithic (free-standing) form. In the first case, the HC powder must be processed to obtain electrodes. This involves mixing the HC, a binder, a conductive carbon, and a solvent to form a slurry, which is then coated on a current collector. However, this step comes with several inconveniences related to the predominant use of the toxic and environmentally risky components such as polyvinylidene fluoride (PVDF) binder and N-methyl-2-pyrrolidone (NMP) solvent, along with multi-step electrode preparation. Therefore, there is a great need to develop more sustainable alternatives. In the case of free-standing HC, the advantage is that no binder, solvent or current collector is used, meaning that it can be used directly as an anode in NIBs. In addition, these materials show potential for a higher energy density due to the fact that the binder/current collector are no longer present. Depending on its architecture, such materials can be engineered into flexible electrodes for different applications, such as wearables.^[18]

Idamayanti et al.^[19] reported a free-standing HC anode obtained from cellulose nanocrystals (CNCs), reinforced with a chitosan substrate. The electrodes were obtained by mixing commercial HC powder, chitosan solution, CNCs, and conductive additive and poured into molds to obtain the binder-free self-standing films. These materials could deliver an iCE of 82% and a reversible capacity of 233 mAh g⁻¹ at a current density of 25 mA g⁻¹, when tested in NIBs. In another study, Gao et al.^[20] reported a flexible self-supporting soft carbon fibers anode made out of PAN (polyacrylonitrile), using wet spinning approach and different pyrolysis temperatures: 800, 1250 and 2350 °C. When used as anodes in NIBs, the materials delivered capacities between 75 and 190 mAh g⁻¹ at a current density of 30 mA g⁻¹. By using the same precursor, PAN, but mixed with different contents of carbon dots, Guo et al.^[21] prepared self-standing HC electrodes heat-treated at 1100 °C. The best material exhibited a reversible capacity of 214 mAh g⁻¹ at 20 mA g⁻¹ and an iCE of 72%. Biomass waste cotton fabrics and spent masked were also used for the fabrication of binder-free electrodes.^[22,23] The best performance was achieved for the highest pyrolysis temperature (1300 °C), that is, iCE of 86%, reversible capacity of 280 mAh g⁻¹ at 20 mA g⁻¹ in 1 M NaPF₆ in diglyme, and good stability for 300 cycles.^[23]

Self-standing HC electrodes (SSEs) present some limitations as well, in particular the low mechanical stability, the difficult electrolyte wetting for dense films, and a lower conductivity due to the absence of conductive additive. To overcome some of these drawbacks, a coating has been proposed to improve the electronic conductivity and/or tune the surface properties. A sputtered layer of gold was applied to cellulose-derived binder-free SSE, improving both the iCE (from 82% to 85%) and the reversible specific capacity (from 240 to 300 mAh g⁻¹) of the electrodes.^[24] Coating SSE with soft carbon derived from coal pitch was shown to limit the formation of defects and oxygen-based functional groups, which minimizes the side reactions and the excessive

formation of SEI. This results in a high iCE of 94.1%, a high capacity of \approx 300 mAh g⁻¹ in 1 M NaPF₆ in a 1:1 EC/DMC and improved cycle stability.^[25] A brief summary of the state of the art of pristine and C-coated SSEs, including information on the precursors used, the pyrolysis process, and electrochemical performance, is presented in Table S1, Supporting Information.

Although C-coating has been applied on several HC powders,^[26–28] there are only limited works done on SSE (Table S1, Supporting Information). Usually, chemical vapor deposition (CVD) process with gases or liquids is used, since it offers control over the carbon layer (e.g., homogeneity, thickness, and structure). CVD-grown carbon layers improve the charge transfer kinetics by providing conductive pathways for electrons and ions. A uniform C-coating with low porosity minimizes the electrolyte decomposition and side reactions, improving iCE and extending cycle life.^[26,29,30] Among CVD techniques, plasma enhanced (PE)-CVD presents several advantages, including homogeneity of the coating, large area deposition, and possibility to use lower temperatures of deposition. This technique has been used to obtain bulk nanocrystalline graphite (bNCG) thin films, as well as nanocrystalline graphite nanowalls morphology, as reviewed elsewhere.^[31] They are composed of turbostratic nanocrystalline domains of sp² hybridized carbon encompassed in an sp³/amorphous matrix, with a ratio sp²/sp³ > 1 providing a high electrical conductivity and high stability.

Despite the interest of this technique, to our knowledge, there is no work reporting the deposition of nanocrystalline graphite on HC materials for Na-ion battery applications. In this work, the advantages of binder-free electrodes are combined with those of C-coating by exploring the impact of SSE pyrolysis temperature on C-coating growth by PE-CVD, as well as the role of post-treatment temperature on the resulting material properties and electrochemical performance. C-coating enhances both the iCE (up to \approx 93%) and rate capability by reducing the structural defects and increasing the electronic conductivity.

2. Experimental Section

2.1. Material Synthesis

2.1.1. SSE Preparation

The preparation process of HC SSEs (illustrated in Figure 1) is inspired from our previous work,^[24] however, several important modifications were included (a different filter paper (FP) precursor, a different pyrolysis temperature/duration, and the removal of the impregnation step with phenolic resin). Whatman cellulose-based filter paper—Grade 3 (with a thickness of 390 µm) was used as the precursor to fabricate the HC SSE. First, the FPs, with an appropriate diameter, *d* of 1.6 cm obtained after punching, were sandwiched between two alumina plates and pyrolyzed at 900 °C for 1 h, followed by natural cooling, to obtain G3_900 materials. The G3_900 was also pyrolyzed between glassy carbon plates at 1500 °C for 3 h to obtain the G3_0 (*d* = 1.1 cm).

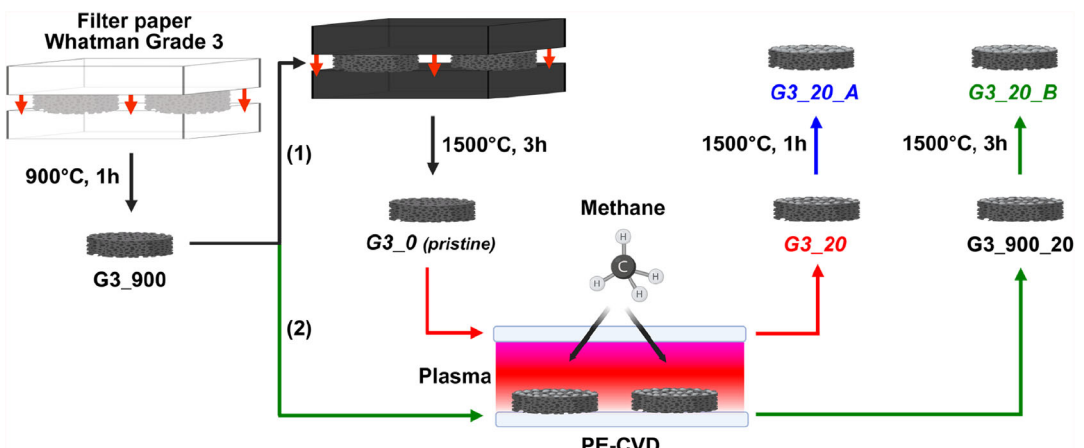


Figure 1. Scheme of the synthesis process of pristine (G3_0) and graphite coated (G3_20, G3_20_A, and G3_20_B) hard carbon binder-free self-standing electrodes via PE-CVD.

2.1.2. Carbon Coating by PE-CVD

The G3_0 and G3_900 carbon electrodes were coated with a thin layer of NCG via a previously established PE-CVD process, with a few small adjustments,^[31,32] with the Nanofab1000 system (Oxford Instruments, Abingdon, UK). The carbon electrodes were placed on a Molybdenum carrier and immobilized via diced Si strips on each side. The carrier was then introduced in the PE-CVD reactor via a load-lock and placed on the preheated bottom electrode (@ 650 °C). The substrate temperature is then raised to 900 °C at a rate of $\approx 15^\circ \text{ min}^{-1}$ in an Ar:H₂ atmosphere. After a 15 min annealing step in the same Ar:H₂ atmosphere at 900 °C, the plasma growth step takes place. The plasma is ignited in a CH₄:H₂ (60:75 sccm) atmosphere at a pressure of 1500 mTorr and 100 W RF discharge power. After a 20 min growth step, the substrate temperature is reduced to 650 °C at a rate of $\approx 10^\circ \text{ C min}^{-1}$ and the carrier is evacuated to the load-lock where it further cools down to room temperature. Three HC SSEs are coated simultaneously, and the process is repeated on both sides of the carbon discs (20 min on each side) for each deposition process, totaling in a 40-min deposition. The obtained C-coated samples denoted G3_20 (originating from G3_0) and G3_900_20 (originating from G3_900) are either used directly as SSEs or underwent another thermal treatment, as described below.

2.1.3. Post- PE-CVD Thermal Treatment

Furthermore, an additional post-PE-CVD thermal treatment was carried out at 1500 °C for 1 h with both G3_20 and G3_900_20, to enhance the graphitization of the C-coating on the electrode surface. All thermal treatments were performed in the same Argon atmosphere (flow rate = 15 L h⁻¹) and the samples are denoted G3_20_A and G3_20_B. In the end, four HC SSEs were obtained and discussed in detail: pristine G3_0 and graphite-coated G3 (G3_20, G3_20_A, and G3_20_B), while the intermediate materials (G3_900, G3_900_20, and G3_0) will be briefly discussed in some specific parts of the manuscript.

2.2. Material Characterization

The structure of SSEs was analyzed by X-ray diffraction (XRD) and Raman spectroscopy. Bruker D8 Advanced diffractometer with a flat-plate Bragg-Brentano $\theta-\theta$ geometry, equipped with a Copper anticathode ($\lambda = 1.5406 \text{ \AA}$), was used to obtain XRD diffractograms in the 2θ range from 10° to 90°. By applying Bragg's law, formula (1), to the (002) plane peaks, the graphene interlayer spacing (d_{002}) was determined

$$2d \sin \theta = n \cdot \lambda \quad (1)$$

In addition, the Scherrer equation,^[33] according to formula (2), was applied to the XRD peaks of the (002) and (100) planes, respectively, to estimate the crystallite height (L_c) and crystallite width (L_a) values.

$$L_{(a,c)} = \frac{k \cdot \lambda}{\text{FWHM} \cdot \cos \theta} \quad (2)$$

where $k = 0.9$ for L_c and 1.84 for L_a ; FWHM is the full width at half-maximum intensity; λ is the X-ray wavelength. Moreover, by using the L_c value, the number of stacked graphene layers (N) was calculated using the following formula:

$$N = \frac{L_c}{d_{002}} + 1 \quad (3)$$

Raman analyses of the SSEs were conducted using a LabRAM 300 spectrometer (Horiba Jobin-Yvon), equipped with a continuous wave (CW) diode-pumped solid-state laser ($\lambda = 523 \text{ nm}$). The instrument parameters, such as filter—D1, objective lens—50× and acquisition time—60 s, were set before the analysis. Mapping mode was selected to collect nine Raman spectra in different points on a selected region for each sample, and the average spectrum was used for further exploitation. The area values as well as the FWHM of the D and G peaks were determined through spectral fitting with a combination of Gaussian-function for peak G and Lorentz-function for the D band. The latter was fitted with three peaks: D1, D3, D4 with $R^2 > 0.98$, according to a modified

procedure compared to that described the literature.^[34] The area ratio of D_1 and G bands (I_{D_1}/I_G) and the $\text{FWHM}_{D_1}/\text{FWHM}_G$ ratio were used to evaluate the disorder degree of the HC material. The high-resolution scanning electron microscope (HR-SEM) Nova NanoSEM 630 (FEI Company, Hillsboro, OR, USA), equipped with a Schottky field emission gun, was used to observe the morphology of the SSEs before and after C-coating. A conventional Everhart-Thornley detector for magnifications of up to 10,000 \times and a through-lens detector for magnifications of up to 400,000 \times at 10 kV accelerating voltage were used. In addition, high-resolution transmission electron microscopy (HR-TEM) images were obtained with a JEOL ARM-200F apparatus operating at 200 kV, which provide further information on the local structure of the materials. The samples were ground in a mortar with chloroform to obtain fine powder that was laid on a carbon grid for analysis. X-ray photoelectron spectroscopy (XPS) analyses were carried out on two SSEs (G3_0 and G3_20_B) in the region of 200–1200 eV, using a VG Scienta SES 2002 spectrometer equipped with a monochromatic X-ray source (Al Kalpha = 1486.6 eV) and a G Scienta XM780 monochromator. The analytical results were used to evaluate and compare the surface chemical composition of the electrodes before and after graphite coating.

2.3. Electrochemical Characterization

First, the SSEs (surface of $\approx 0.95 \text{ cm}^2$ and mass loading of 4.8–6.0 mg cm $^{-2}$) were placed in a Büchi oven, dried at 120 °C for 12 h, under vacuum, to completely remove moisture, and then transferred to an argon-filled glove box. Here, half-cells were assembled into CR2032-type coin cells, using HC SSEs as working electrode, two glass fiber (Whatman GF/C, $d = 1.6 \text{ cm}$) as separator, and sodium metal (Sigma-Aldrich, 99.9% purity, $d = 1.2 \text{ cm}$), as both counter and reference electrode. The electrolyte used in the electrochemical tests was 1 M NaPF $_6$ dissolved in a mixture of ethylene carbonate (EC) and dimethyl carbonate (DMC) solvents, in equal volume ratios, with 2% fluoroethylene carbonate (FEC) additive. The electrochemical tests, using a BCS-805 battery cycler (BioLogic), were performed in a voltage window from 0.005 to 2.1 V (vs. Na $^+$ /Na) to determine the performance of the electrodes. The galvanostatic cycling with potential limitation (GCPL) test was carried out in three steps. The Na $^+$ insertion process consisted of: 1) a galvanostatic step (constant current at 0.1C) in the voltage range of 2.1–0.005 V versus Na $^+$ /Na, and 2) a potentiostatic step (constant voltage at 5 mV vs. Na $^+$ /Na) until 0.01C was reached. This was followed by Na $^+$ extraction, when 3) the current was reversed and another galvanostatic step, at 0.1C in the voltage of 0.005–2.1 V, was performed to complete one cycle. A current density of 37.2 mA g $^{-1}$ (0.1C) was applied for the first five cycles and then changed to 372 mA g $^{-1}$ (1C). Retention rate was determined considering the seventh (once the cell is stable at 1C rate) and the 50th cycles. Rate capability tests were carried out using symmetric and asymmetric conditions. For symmetric conditions, the C-rate of steps 1), 3) was

changed as follows: 0.1C, 1C, 2C, 3C, 5C, 10C and return back to 0.1C, while for asymmetric conditions the C-rate of step 1) was kept constant at 0.1C while the C-rate of step 3) was changed as follows: 0.1C, 1C, 2C, 3C, 5C, 10C, and return back to 0.1C. Note that each C-rate was maintained for five cycles. In addition, Nyquist electrochemical impedance spectroscopy (EIS) analyses on the pristine SSE (G3_0) and the representative graphite-coated SSE (G3_20_B) were performed, using a VSP-300 multichannel potentiostat (BioLogic), to evaluate the effect of the graphite coating on the resistance and interfacial phenomena. The measurements were carried out before cycling and at different states of cycling: after one cycle at 0.1C (SEI formation), after five cycles at 0.1C (stabilized SEI layer), and after five additional cycles at 1C (to check SEI layer stability after switching from 0.1 to 1C).

3. Results and Discussion

3.1. Physicochemical characterization

Following synthesis, physicochemical and electrochemical characterizations were performed on the SSEs G3 pristine (G3_0) and G3 graphite-coated (G3_20, G3_20_A, G3_20_B), in order to evaluate the influence of the coating process, as well as the impact of the post-pyrolysis process, on the properties and performance of the SSEs. XRD analyses were performed to provide information on the structural properties of the materials. The XRD diffractograms (Figure 2a) show three broad diffraction peaks—two intense peaks located at 2θ of $\approx 23^\circ$ and 43° , and one weak peak at $2\theta \approx 80^\circ$ —corresponding to the (002), (100/101), and (110) graphite planes, respectively.^[35] Such broad peaks indicate disordered materials, which is typical of HCs. For the (002) peaks, a slight shift towards higher 2θ values can be observed for the graphite coated samples (G3_20, G3_20_A, and G3_20_B) compared to the pristine sample (G3_0). This results in smaller d-spacing values for 002 plane (Table 1) for G3_20 (3.798 Å), G3_20_A (3.789 Å) and G3_20_B (3.769 Å) compared to those of G3_0 (3.809 Å).

Although the difference in d_{002} values is not significant, the decrease noticed suggests that the graphite coating contributes to the increase in the structural order of SSEs. Furthermore, since the minimum d_{002} spacing required for the insertion of Na $^+$ in HC is 0.37 nm,^[36] the sodium ion storage and transport capacity of all four SSEs is favorable, as their d_{002} values exceeds this minimum threshold. The pseudo-graphite domain sizes (crystallite height and width) based on the (002) and (100/101) peaks, respectively, were determined by applying the Scherrer equation (Equation 2).^[33] The values for the height of the stacked graphene layers ($L_c = 11.2$ – 11.6 \AA) are not too different between the samples, however, a slight increase is noticed for the post-thermal treated SSEs (Table 1).

According to the formula (3) and based on the d_{002} and L_c , the pseudo-graphite domains of the four SSEs were determined to consist of ≈ 4 stacked graphene layers (N). Furthermore, the

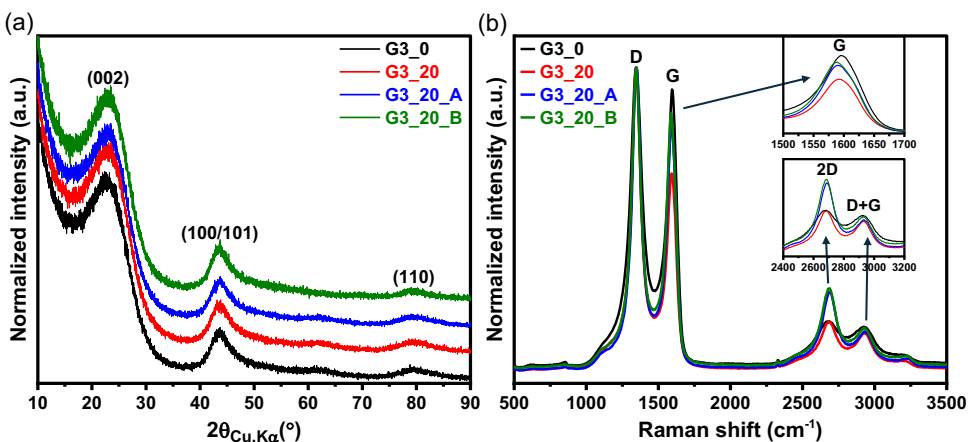


Figure 2. Structural characterization of pristine (G3_0) and graphite coated (G3_20, G3_20_A, and G3_20_B) hard carbon SSEs: a) XRD diffractograms and b) Raman spectra normalized based on *D* band with the zoom-in images of *G*, *2D* and *D* + *G* peaks (inset).

Table 1. Characteristics of pristine (G3_0) and graphite-coated (G3_20, G3_20_A, and G3_20_B) hard carbon SSEs, including the interlayer spacing (d_{002}), crystallite height (L_c) and width (L_a), and disorder degree (I_{D1}/I_G and $\text{FWHM}_{D1}/\text{FWHM}_G$).

Sample name	$d_{002}^{\text{a})}$ [Å]	$L_c^{\text{a})}$ [Å]	$L_a^{\text{a})}$ [Å]	$I_{D1}/I_G^{\text{b})}$	$\text{FWHM}_{D1}/\text{FWHM}_G^{\text{b})}$
G3_0	3.809	11.2	35.4	2.44	1.43
G3_20	3.798	11.2	38.8	2.58	1.06
G3_20_A	3.789	11.6	39.3	1.95	1.02
G3_20_B	3.769	11.3	37.3	1.92	1.05

^{a)}Determined by XRD. ^{b)}Determined by Raman spectroscopy.

graphite coating and the post-pyrolysis process appear to significantly impact the width of the stacked graphene layers (L_a), which tends to increase in the following order: G3_0 (35.4 Å) < G3_20_B (37.3 Å) < G3_20 (38.8 Å) < G3_20_A (39.3 Å).

Additional information regarding the local structure of the electrodes was obtained by Raman spectroscopy (see Figure 2b and S1 in the Supporting Information). All materials exhibit two main peaks that are characteristic of hard carbon: the *D* band (1348 cm⁻¹), which is related to breathing modes of sp²-bonded atoms in hexagonal rings that are activated by defects, edges, and disorder; and the *G* band (~1590 cm⁻¹), which is associated with sp²-bonded carbon in graphite-like structures (rings and chains).^[37,38] A closer inspection of the *G* band (inset Figure 2) allows to observe a shift of the maximum peak position of G3_0 (1597 cm⁻¹) toward lower wavenumbers after the deposition of carbon by PE-CVD (1592 cm⁻¹ for G3_20) and post-annealing at 1500 °C of the deposited carbon (1589 cm⁻¹ for G3_20_A and G3_20_B).

This suggests that additional graphene-like layers have been deposited on the surface of the SSEs.^[39,40] It is worth noting that the *G* band intensity of G3_20 is the lowest which would suggest, at a first glance, that the layer deposited by PE-CVD at 900 °C contains less C sp² than the other materials. The calculated ratio between the *D1* and *G* bands (I_{D1}/I_G) is generally used to

determine the degree of disorder; in crystalline materials, a higher ratio indicates smaller crystallites and larger structural defects. The values obtained (see Table 1) are slightly lower for the pristine material (G3_0 ≈ 2.44) than the electrode after PE-CVD with no post-treatment (G3_20 ≈ 2.58), leading to the same conclusion that the latter material is more disordered. However, for accurate interpretation of Raman spectra, it is important to consider not only the peak's intensity (related to the number of graphitic domains), or I_{D1}/I_G (related to the degree of disorder), but also the peak's width (associated with the distribution and homogeneity of graphitic domains), thus, narrow peaks implying more graphitic domains and less disorder. In fact, the *G* band of G3_20 is the narrowest one and the ratio of the FWHM of the *D1* and *G* bands shows a significantly lower value for G3_20 than for G3_0 (1.06 vs. 1.43). This suggests that G3_20 has less C sp² domains (smaller *G* band intensity), but with larger surface and a more homogeneous distribution of defects (narrower *G* band).^[37] The opposite trend between I_{D1}/I_G and $\text{FWHM}_{D1}/\text{FWHM}_G$ could indicate that the defect density and structural disorder do not increase proportionally, or that different types of defects impact the *D* and *G* the bands differently.^[39] However, when post-thermal treatment at 1500 °C is performed (G3_20_A and G3_20_B), both the I_{D1}/I_G and the $\text{FWHM}_{D1}/\text{FWHM}_G$ decrease, indicating an increase in the structural order of the materials, with more C sp² domains that are homogeneously distributed.

Further insights were obtained by fitting the Raman spectra according to the Sadezky et al.^[34] procedure, as shown in Figure S1, Supporting Information. The D4 band, which is often associated with C sp²–C sp³ bonds and/or C–C and C=C stretching vibrations in linear carbon chains (such as polyenes),^[41,42] mainly decreases after thermal annealing (G3_20_A and G3_20_B). Additionally, the intensity of the D3 band, which is located between the *D1* and *G* bands, decreases after carbon coating (G3_20) and thermal annealing, indicating a reduction in the fractions of amorphous carbon and functional groups.^[34] Taken together, these results suggest that the structural features of

the electrodes improve slightly after the CVD coating, while supplementary thermal annealing increases the structural order.

This increase in graphitization level is also supported by the second-order 2D Raman peak (2700 cm^{-1}), which is associated with graphitic domains and increases in intensity following C-coating (G3_20) and, in particular, post-annealing (G3_20_A and G3_20_B). There is no significant difference noticed in the structure of G3_20_A and G3_20_B.

The morphology of pristine SSE and C-coated SSE was studied using the SEM technique, as illustrated in Figures 3 and 4. Images of pristine G3_0 (Figure 3) at low magnification reveal a woven carbon network consisting of interconnected fibers and macro-porosity. This porosity may be beneficial for electrochemical performance since it can enhance the electrolyte adsorption and diffusion through the material. The fibers diameter is rather heterogeneous, ranging from 1 to $20\text{ }\mu\text{m}$, while the fibers length, although difficult to be determine precisely, it exceeds $500\text{ }\mu\text{m}$. Some thin fibers resembling a spider's web are also observed between the main larger fibers. At higher magnification, the fiber appears rather smooth in the surface.

When C-coating is performed on the pyrolyzed sample at $1500\text{ }^\circ\text{C}$ (G3_20_A), the fibers' surface becomes rougher, indicating the formation of a continuous thin film with tightly packed domains of fairly uniform size (\approx tens of nanometers), visible throughout the surface (Figure S2, Supporting Information). The grain size of the C-coating film, is homogeneously distributed on the fibers, with a few large nanoparticles visible in some places. When the C-coating is performed on the SSE pyrolyzed at $900\text{ }^\circ\text{C}$ (G3_20_B), a similar homogeneous distribution of small grains is observed on the surface, although in this case, larger

nanoparticles become more prevalent on the surface (see Figure 4). This observation would suggest that carbon growth is more significant in this sample, which may be due to the fact that the film prepared at $900\text{ }^\circ\text{C}$ has a higher N_2 specific surface area ($400\text{ m}^2\text{ g}^{-1}$) and richer surface chemistry (4.1 at% O) than that prepared at $1500\text{ }^\circ\text{C}$ ($34\text{ m}^2\text{ g}^{-1}$ and 2.31 at%), in agreement with other works.^[11] These characteristics act as active sites, favoring interactions with decomposed methane gas molecules and promoting the deposition of thicker carbon layers.

The grain size distribution within the bNCG C-coating was further determined by analyzing ≈ 200 grains from the higher magnification ($400,000\times$) SEM images over a $750 \times 710\text{ nm}^2$ area with the ImageJ software (NIH). The grain size of the PE-CVD coating ranged from 7 to 22 nm for the G3_20_A sample and from 8 to 19 nm for G3_20_B sample. The resulting size distribution histograms (Figure S3, Supporting Information) were best fitted with a Gaussian function. The majority of grain sizes in both samples were within the $10\text{--}16\text{ nm}$ size range, with a mean lateral size of $14 \pm 3\text{ nm}$ for G3_20_A and $13 \pm 3\text{ nm}$ for G3_20_B (Table S2, Supporting Information). The G3_20_B SSE was additionally investigated at a lower magnification ($100,000\times$) over a $3 \times 2.84\text{ }\mu\text{m}^2$ area to determine the size of the larger nanoparticles observed on the C-coating surface. Approximately 100 such nanoparticles were investigated with the ImageJ software. The respective particles have a mean lateral size of $26 \pm 11.7\text{ nm}$, distributed over a much wider range, from 8 to 57 nm (Figure S4, Supporting Information).

Additionally, cross-section SEM investigations were performed on both G3_20_A and G3_20_B to analyze the relative fibers' surface coverage within the porous SSEs. A total of

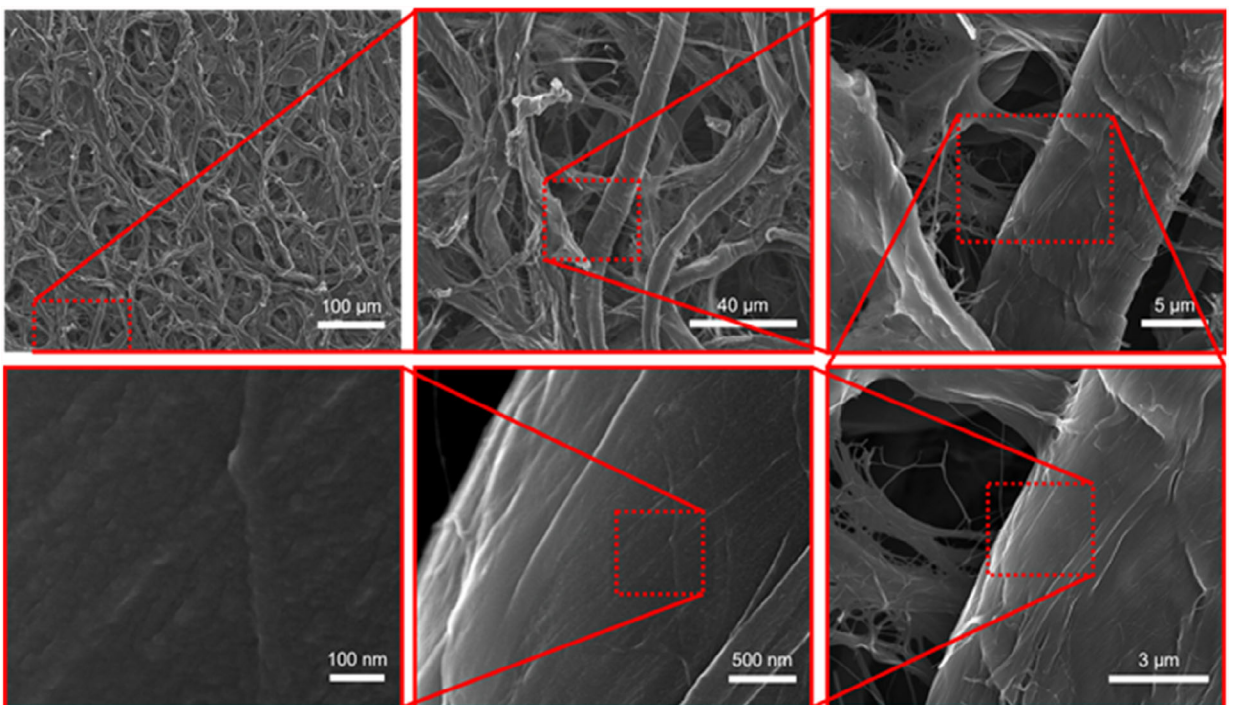


Figure 3. SEM micrographs of pristine hard carbon SSE (G3_0) at different magnifications: $500\times \rightarrow 2000\times \rightarrow 10,000\times \rightarrow 25,000\times \rightarrow 100,000\times \rightarrow 400,000\times$.

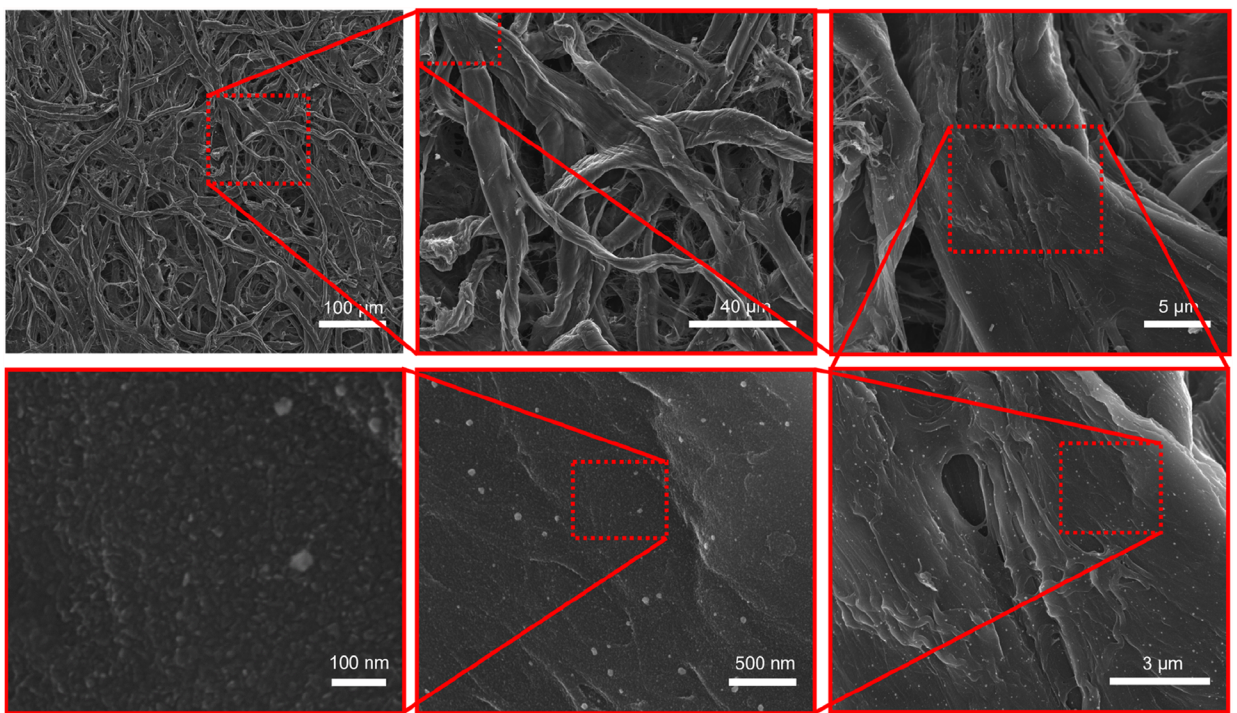


Figure 4. SEM micrographs of graphite-coated hard carbon SSE (G3_20_B) at different magnifications: 500 \times → 2000 \times → 10,000 \times → 25,000 \times → 100,000 \times → 400,000 \times .

eleven quantitative measurements were performed on each sample to evaluate the surface coverage, starting from the surface and up to a depth of \approx 95 μm , which is roughly the middle of the SSEs. The fill factor was estimated using the ImageJ software to ensure accurate and consistent evaluation. The use of cross-sectional imaging, combined with quantitative analysis, enabled a more comprehensive assessment of the vertical

distribution and penetration depth of the bNCG layer within the porous matrix, offering valuable insight into the conformality and effectiveness of the C-coating throughout the samples' thickness. Both G3_20_A (Figure S5, Supporting Information) and G3_20_B (Figure 5) appear to have a good surface coverage of the fibers, with a fill factor of around 100%, up to a depth of \approx 65 μm .

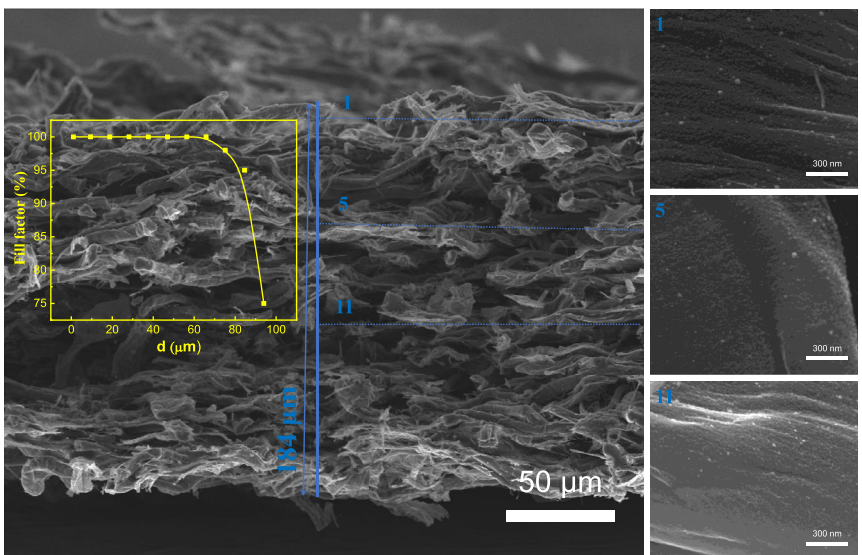


Figure 5. Cross-sectional SEM micrographs of the G3_20_B SSE. **Left:** cross-section SEM at 1000 \times magnification of the entire SSE, with three representative points from different regions marked for localized analysis. The inset presents the relative surface coverage (fill factor) in each selected area. **Right:** cross-section SEM at 200,000 \times magnification of the marked areas.

At larger depths, between 70 and 90 µm, a slight drop is observed for the fill factor in both cases, the relative surface coverage dropping to 95% for G3_20_B and to 89% for G3_20_A. Near the middle of the samples, at around 94 µm depth, a steep decline of the fill factor to 75% is observed for G3_20_B, while for G3_20_A it drops to 56%. This further confirms the enhanced growth of the bNCG thin film on the G3_20_B sample, which was pyrolysed at 900 °C. Overall, the analysis shows a good conformality of the PE-CVD process almost throughout the entire thickness of the SSEs, with a slight drop-off towards the middle of the samples, more in the case of the G3_20_A SSE. As the deposition process is plasma-assisted, the lower surface coverage towards the middle of the samples can be attributed to a lower growth rate due to either a radical diffusion limitation or ion shadowing. Taking into account the porous nature of the SSEs and observing that the fill factor begins to decrease only after a depth of \approx 65 µm, it suggests that the growth rate near the middle of the SSEs is more likely limited due to diffusion. If ion shadowing would have been the dominant limiting factor, the surface fill factor would be expected to decrease sooner, at a lower depth. The SEM investigations ultimately suggest that the PE-CVD C-coating has a higher growth rate on the sample pyrolyzed at 900 °C, which would entail a higher thickness of the bNCG thin film on the SSE's fibers.

The local structure of the materials analyzed by TEM shows the PE-CVD carbon between the fibers as aggregates of 0.5–1 µm (Figure S6, Supporting Information). These aggregates, which are made up of very small crystalline nanoparticles (see Figure 6), represent the C-coating film that may have broken during the grinding process used to prepare the sample for TEM analysis. The measured spacing of 0.21–0.24 nm corresponds to the (100) plane of graphite, which reflects the in-plane atomic arrangement within the graphene layers. In addition, the typical hard carbon structure is observed on pristine G3_0 (Figure S7a,

Supporting Information), consisting of short pseudo-graphitic domains gathering 3–4 stacked graphene layers and numerous closed pores. When PE-CVD carbon is deposited on samples that have been pre-treated at 1500 °C, fewer pseudo-graphitic domains are observed (G3_20, Figure S7b, Supporting Information). However, a further post-treatment at 1500 °C (G3_20_A, Figure S7c, Supporting Information) allows longer pseudo-graphitic layers to form, which is consistent with the higher L_a value obtained by XRD. Many closed pores are observed also on G3_20_A, which is different than G3_20_B material pre-treated at 900 °C. Therefore, the graphite layer deposited by PE-CVD process on the sample treated at 900°C seems to prevent the formation of closed pores during the subsequent post-thermal treatment at 1500 °C. As shown in the literature, the CVD carbon can block or fill the micropores, resulting in a reduction of overall microporosity and specific surface area.^[26,43] Such carbon that fills the micropores, might inhibit the rearrangement or closure of these pores during post-thermal treatments at high temperatures (1500 °C),^[43] which usually causes the transformation of open micropores into closed pores within the carbon matrix.^[44] However, our measurements revealed that the N₂ SSA of the pristine material, G3_900 (400 m² g⁻¹) does not diminish after the PE-CVD, G3_900_20 (560 m² g⁻¹, Table S3, Supporting Information), on the contrary, it increases due to the presence of the graphite nanoparticles on the material's surface. The differences between the two deposition processes may explain this result. PE-CVD operates at low pressure (1500 mtorr) and high temperature (900 °C), whereas CVD occurs at atmospheric pressure and lower temperature (\approx 700 °C).^[26,43] The lower pressure and higher temperature in the PE-CVD favor the spreading of gas molecules, limiting their collision. Therefore, molecule-wall collisions dominate in PE-CVD, unlike molecule–molecule collisions in CVD. This mechanism involving collisions with the walls leads to limited

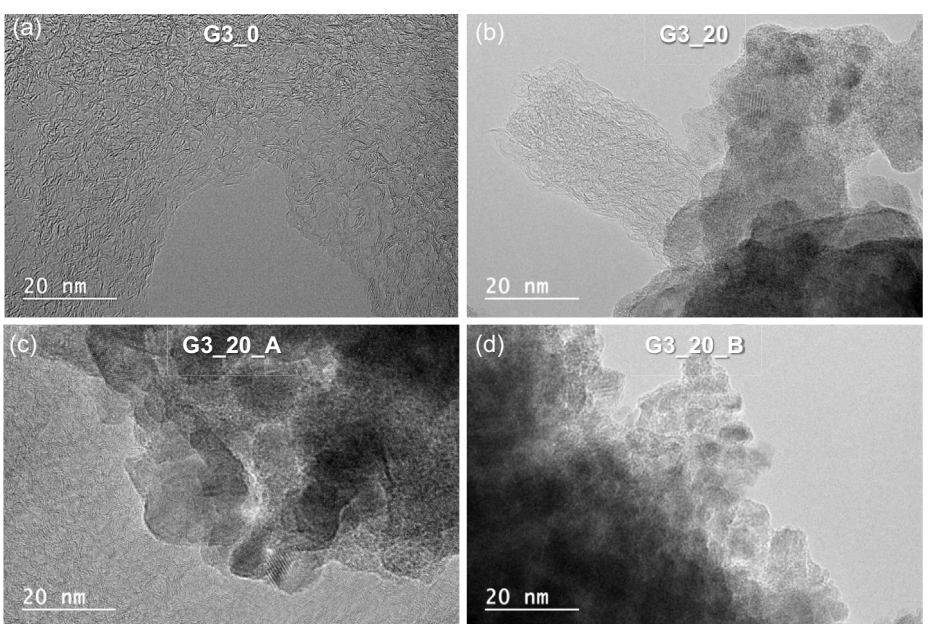


Figure 6. HR-TEM images at 20 nm of hard carbon SSEs : a) pristine (G3_0), and graphite coated b) G3_20, c) G3_20_A, and d) G3_20_B.

diffusion of the precursor gas, which impedes the penetration into narrow micropores and induces the formation of a carbon layer containing graphite nanoparticles, instead of filling the micropores.^[45,46] This happens, when pore diameter is smaller than the mean free path of the gas molecules (the average distance a gas molecule travels before colliding with another molecule).^[47] Therefore, in the PE-CVD carbons, the presence of the graphitic layer on material's surface prevents the folding and bending of the carbon layers required to form closed pores.^[48] In contrast, pore filling impedes closed pore formation in CVD. However, more studies are required to fully understand the closed pore suppression induced by C-coating.

Although the Na-ion storage mechanisms are still under debate, both the graphitic domains and the closed pores are usually considered as very important to increase the Na-storage via insertion and/or a filling mechanisms occurring in the low voltage plateau (<0.1 V).^[49,50]

XPS analyses performed on pristine G3_0 and C-coated G3_20_B materials are shown in Figure 7. The chemical composition (after subtraction of small Al-traces coming from the pyrolysis boat) reveals a similar amount of C (97.69 at% vs 97.98 at%) and O (2.31 at% vs 2.02 at%), with the C-coated material having a slightly richer carbon at% in the surface (Figure 7a). The comparison of the high resolution deconvoluted C 1s profiles (Figure 7b) shows an important contribution at ≈284.3 eV from graphitic C sp² species. The C sp² peak is more intense for the C-coated material, suggesting that more C sp² was formed following PE-CVD, which is consistent with the results of XRD and Raman. In addition, a small fraction of O-functional groups (C-OR, C=O and COOR) is noticed at higher binding energies. Overall, the high carbon content present in the C-coated materials should improve the electronic conductivity, while the low oxygen content should limit the undesirable reactions with the electrolyte.^[11]

3.2. Electrochemical Results

The binder-free hard carbon electrodes were tested in half-cells to evaluate their electrochemical potential in NIBs. The

galvanostatic discharge/charge profiles are presented in Figure 8a and S8a, Supporting Information, and exhibit two distinct electrochemical regions. The first one is the sloping region between 1 and ≈0.05 V, which includes an obvious inflection point around 0.5 V, commonly linked to the formation of SEI.^[51] Below 0.05 V, the profile shifts to a flat plateau region, which is predominant among the two main electrochemical signatures. This plateau is usually related to sodium-ion storage within the graphene interlayer spaces (insertion) and closed pores (filling) of the HC,^[52–55] while the sloping region is associated to sodium-ion adsorption on active sites, defects, open pores, and functional groups of HC.^[56]

During first sodiation at 0.1C, the materials treated at 1500 °C can reach a high specific capacity comprised between 330 and 350 mAh g⁻¹, which is highly reversible (Table 2). More precisely, a reversible capacity of around 320 mAh g⁻¹ is obtained for all materials except G3_20, which has a slightly lower performance of 296 mAh g⁻¹. The materials have a very high iCE, between ≈90% and 92.5% (Table 2), which means that limited irreversible reactions and SEI formation occur during the first cycle. In particular, the two electrodes that undergo a post-thermal treatment at 1500 °C, after the carbon coating, show the highest iCE, which can be associated to a reduction in the surface defects, as revealed by the Raman results (Figure 2).

In terms of stability, Figure 8b shows the results for the first 50 cycles (the first five cycles at 0.1C, followed by 1C). It can be seen that all materials demonstrate excellent stability and similar performance (retention rate between 97.5% and 100%). Furthermore, except for the first cycle and the moment of regime change (0.1C to 1C), the Coulombic efficiency (CE) remains stable at around 100%, indicating a homogeneous and stable SEI layer.^[11]

In contrast, the materials obtained at 900 °C (G3_900 and G_900_20) show a significantly lower iCE (36% and 44%) and capacity (120 and 150 mAh g⁻¹), but demonstrates good cycle stability (Figure S8b, Supporting Information). The reduced performance is associated with their higher SSA, oxygen content and disordered structure compared to the material treated at 1500 °C,

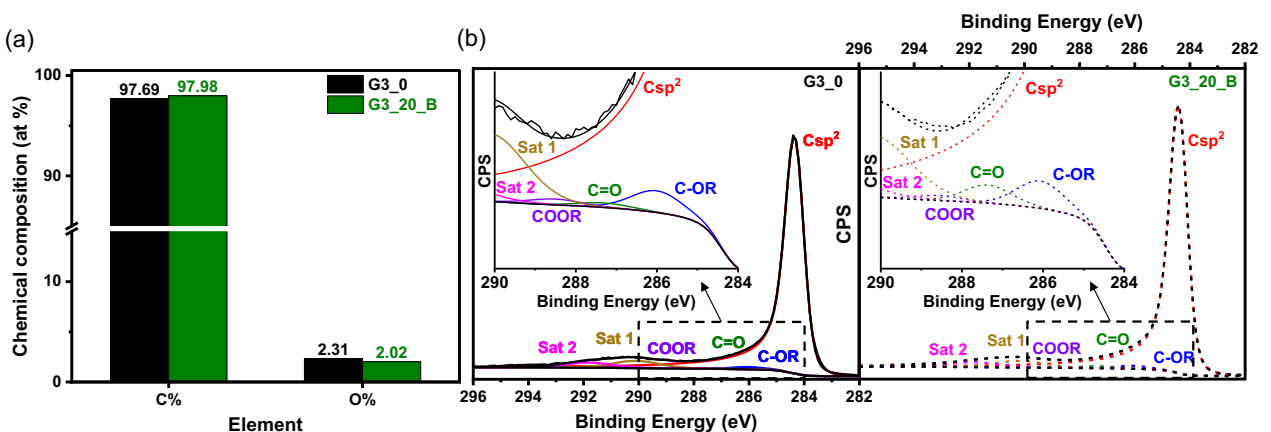


Figure 7. a) XPS chemical composition (C at% and O at%) and b) comparison between C 1s peak of G3_0 (straight line) and G3_20_B (dash line); inset: deconvolution of C 1s peak.

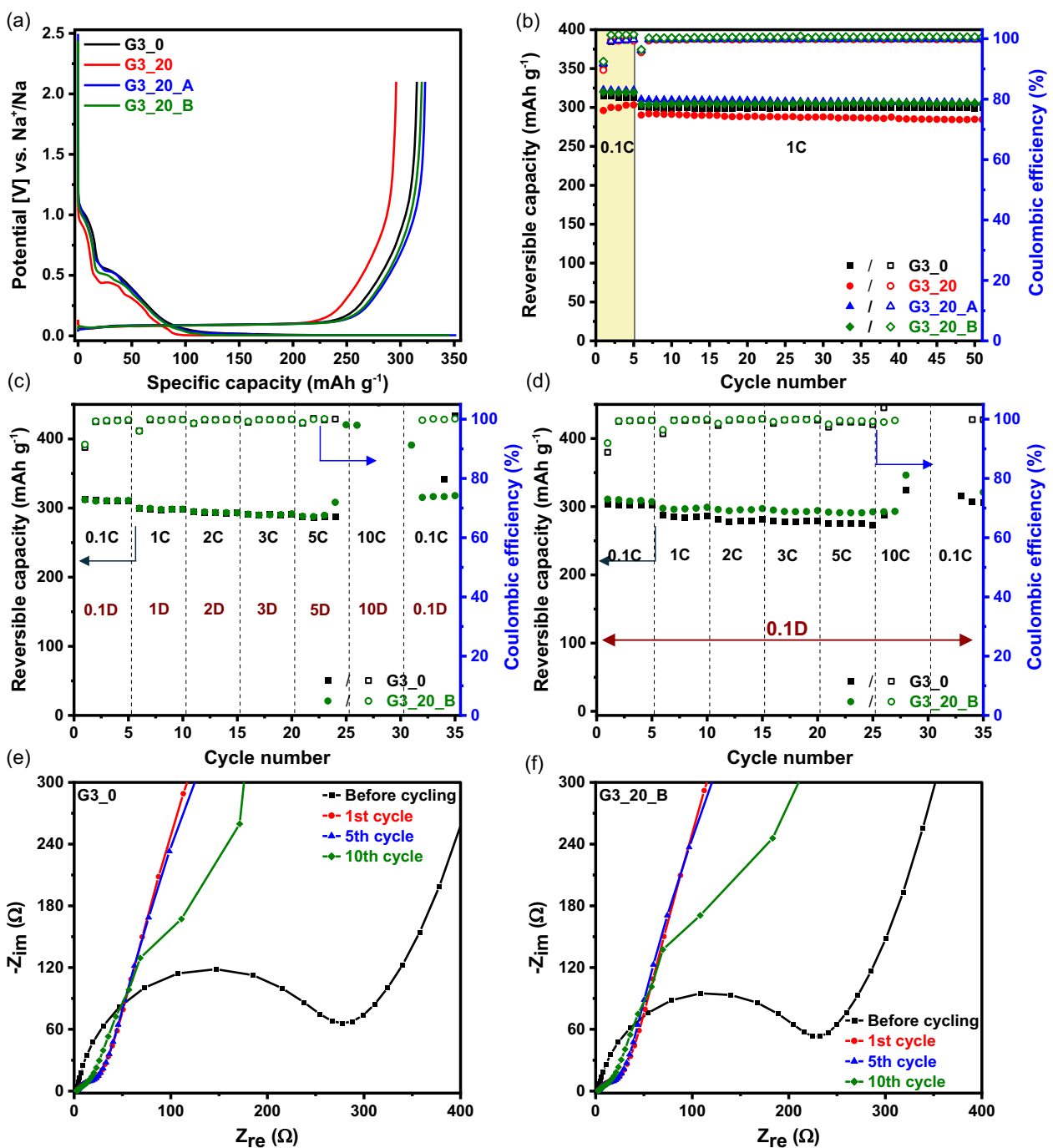


Figure 8. a) 1st discharge-charge cycle of pristine (G3_0) and graphite coated SSEs (G3_20, G3_20_A and G3_20_B), cycled at 0.1C. b) Cycling stability (solid symbol) and Coulombic efficiency (hollow symbol) cycled at 0.1C (yellow area) followed by 1C (white area). C-rate regime tests of G3_0 and G3_20_B: c) symmetrical and d) asymmetrical. Electrochemical impedance spectra of e) G3_0 and f) G3_20_B, measured before electrochemical testing (black line), after testing the material at 0.1C for one cycle (red line) and for five cycles (blue line), and after testing the material at 1C for another five cycles (green line).

G3_0 (see Table S3, Supporting Information). All these drawbacks are eliminated by the post-treatment at 1500 °C, the reason behind our approach.

If one compares these results with those reported in the literature for SSE (Table S1, Supporting Information), it can be seen that the best material proposed in this study deliver

superior performance in terms of iCE, reversible capacity and retention rate. Worth to mention that a slightly superior iCE was reported in a different study (94.1% vs. 92.5%),^[25] however, in the case of G3_20_B the mass loading is five times higher (5.7 vs. 1.2 mg cm⁻²), while the current density applied herein is almost doubled: 37.2 mA g⁻¹ versus 20 mA g⁻¹, (0.1 C rate).

Table 2. Electrochemical performance of pristine (G3_0) and graphite coated (G3_20, G3_20_A and G3_20_B) hard carbon electrodes.

Sample	iCE [%]	1st RC* [mAh g ⁻¹]	1st DC* [mAh g ⁻¹]	CR* after 50 cycles [%]
G3_0	91.1	315.2	346.1	99.9
G3_20	89.6	296.0	330.2	97.5
G3_20_A	91.8	322.9	351.9	98.8
G3_20_B	92.5	319.8	345.9	100

RC* is reversible capacity. DC* is discharge capacity. CR* is capacity retention.

To further explore the benefits of graphite deposition on the electrodes and to better understand the stability of the SEI layer, C-rate tests were performed under different conditions: in a symmetric regime (with the same discharge and charge rates) and in an asymmetric regime (with a constant discharge rate and a variable charge rate). As the materials behaved similarly in terms of cycle stability, only two representative materials were selected for the C-rate tests: G3_0 and G3_20_B.

In the first case, when a symmetric regime is used (see Figure 8c), it is evident that both materials perform remarkably well, up to a 5C rate. The capacity remains stable at around 300 mAh g⁻¹ and the CE is close to 100%, except at the point of changing the cycling regime, when the increase in the applied current density temporarily affects the stability of the SEI and consequently the CE. Besides this transition step, both materials performed very well. Worth mentioning that the potentiostatic step applied plays an important role on maintaining such great performance at high C-rates. It allows enough time to compensate for the slow diffusion kinetics and completely sodiate the HC structure. In contrast, Na⁺ extraction at high currents is characterized by fast kinetics, as confirmed by the high CE values (\approx 100%).

After a few cycles at 5C, important capacity fluctuations are seen in both cases and the increase of C-rate to 10C destabilizes the cells completely. The CE values are also very random and superior to 100%. Interestingly, the transition from 10C to 0.1C allows to recover the stability, the initial reversible capacity (\approx 300 mAh g⁻¹) and the CE (100%) of the G3_20_B material. In contrast, the pristine G3_0 material still exhibits important fluctuations. The loss of capacity stability during fast discharge/charge can be due to sluggish sodium-ion diffusion within the material's pores and interlayer spaces, or to increased polarization.^[57] The graphite coating provides better conductivity, facilitating faster electron transport throughout the electrode.^[58] Furthermore, it stabilizes the SEI, reducing internal resistance and polarization and enabling the electrode to recover its initial capacity.

When tested in the asymmetric regime (Figure 8d), relatively similar behavior was observed, with significant fluctuations present at a 10C rate. However, this time, a slight difference can be seen between the pristine and coated materials. The latter has a slightly higher capacity (e.g., 298 mAh g⁻¹ vs. 281 mAh g⁻¹ at 2C).

In the asymmetric regime, once the materials lose stability, capacity fluctuations appear and none of the materials recover their initial behavior when the C-rate is reduced from 10C to 0.1C. This may be related to side reactions occurring at the electrode/electrolyte interface at high C-rates, leading to excessive SEI growth. This can result in an unstable or thicker SEI that consumes active sodium ions. High-rate cycling can also cause microstructural damage to the materials.^[59] Such changes can permanently block sodium storage sites or hinder sodium-ion diffusion.

Impedance measurements were performed on the two samples to investigate the formation of the SEI layer and establish whether there are any differences between pristine and coated electrodes. Several conditions were considered: before cycling—on the freshly assembled cell, after the first cycle once the SEI layer is mainly formed, after five cycles to give enough time to SEI to stabilize and after 10 cycles, to see the impact of regime change (0.1C–1C).

One can see that for both materials, the high frequency region semicircle (Figure 8e,f) starts almost from 0 ($3\ \Omega$) sign that the bulk/ohmic resistance of the cell is very low. A well-defined semicircle is present for both freshly assembled cells, and it is related to SEI layer formation and charge-transfer resistance.

This clearly suggests that the passivation layer starts to build up simply by putting the HC electrode in contact with the Na metal and the electrolyte, in agreement with other recent findings.^[35] Interestingly, it can be seen that the resistance is higher for G3_0 ($\approx 280\ \Omega$), compared to G3_20_B ($\approx 230\ \Omega$), which suggests sign that the SEI layer is thicker and/or more heterogeneous in the case of the pristine electrode. This explains the improvement in electrochemical performance (i.e., increased iCE and reversible capacity) observed for the two materials that were coated and heat-treated at 1500 °C. This is most likely due to the presence of graphite coating, which reduces SSE defects and provides a homogeneous and stable SEI. It also enhances electronic conductivity, favoring the charge and ion propagation.

Once the first cycle has finished, the impedance has been analyzed again (see the red line in Figure 8e,f), and the resistance has decreased significantly, regardless of the electrode (with G3_20_B showing the least resistance). This suggests that the SEI is well formed, homogeneous and likely more conductive, allowing Na ions to pass more efficiently.

Although the difference is not significant, the passivation layer improves further after the fifth formation cycle as the semicircular resistance decreases slightly (blue line, Figure S9, Supporting Information). This trend continues when the C-rate is increased to 1C (green line, Figure S9, Supporting Information). Therefore, at lower C-rates, the SEI layer is stable and homogeneous, making it favorable for Na⁺ storage. This results in stable performance, as can be seen in Figure 8b. However, once high currents are applied, the integrity of the passivation layer is compromised, significantly affecting the cell's lifespan (Figure 8c,d).

4. Conclusions

Self-standing binder-free hard carbon electrodes were prepared through pyrolysis of cellulose filter paper. The influence of a carbon coating applied via PE-CVD on their properties and electrochemical performance was systematically investigated. Methane decomposition during PE-CVD resulted in the formation of a continuous nanocrystalline graphitic film, which deposited conformally on the surface of the electrodes. SSE pyrolyzed at 900 °C forms a thicker C-coating, with more surface nanographitic particles than the one pyrolyzed at 1500 °C. This graphite film deposited on 900 °C-SSE impedes closed pore formation during post-pyrolysis at 1500 °C. In contrast, direct pyrolysis at 1500 °C enables the development of closed pore, which are not affected by the further deposition of graphic film (G3_20_A). The post-annealing treatment at 1500 °C significantly improved the crystallinity of the C-coating on both materials. It reduced structural defects, mitigating undesirable interfacial reactions and resulting in a more homogeneous and conductive SEI. This process resulted in an increase in iCE, achieving a value as high as 92.5%. Additionally, the enhanced electronic conductivity provided by the nanographitic carbon coating and the stable SEI led to a modest improvement in rate capability.

In summary, the C-coated SSE demonstrated both a high iCE and a reversible capacity of 320 mAh g⁻¹, along with excellent cycling stability, maintaining ≈100% capacity retention over 50 cycles. Notably, the primary benefit of the carbon coating was the marked increase in iCE, which remains a critical parameter for optimizing NIBs. The performance is similar regardless of the pyrolysis temperature used to prepare the SSE. The superior conductive carbon coating and better coverage in G3_20_B outweigh the beneficial effect of closed pore formation in G3_20_A. This suggests that the pyrolysis step could be performed at a lower temperature (900 °C instead of 1500 °C), thereby reducing energy consumption. In addition, the SSE pyrolysed at 900 °C promotes a higher growth rate of the PE-CVD coating, which would allow for a shorter plasma growth step to develop a coating of a similar thickness as for the SSE pyrolysed at 1500 °C, reducing energy consumption even further. Overall, this study demonstrates a sustainable approach for synthesizing HC electrodes from renewable resources, eliminating the need for binders, solvents and current collectors. The application of a C-coating further enhances electrode performance, highlighting the potential of this fabrication strategy for advanced energy storage systems.

Acknowledgements

This work was performed in the frame of RS2E (French research network on electrochemical energy storage). The project received funding from Région Grand Est (project no. 23-DOC-109), ANR (ANR-10-LABX-76-01, STORE-EX and ANR-22-PEBA-0003, PEPR Battery - HipoHyBat) and the Romanian Ministry of Research, Innovation and Digitization through the Core Program, project no. 23070201, within the National Plan for Research,

Development, and Innovation 2022–2027. The authors acknowledge Dr. Jean-Marc Le Meins (XRD) Dr. Samar Garreau (XPS) and Dr. Cyril Vaulot for the help provided with the hard carbon characterization via IS2M technical platforms.

Conflict of Interest

The authors declare no conflict of interest.

Data Availability Statement

The data that support the findings of this study are available from the corresponding author upon reasonable request.

Keywords: C-coating • hard carbon • Na-ion batteries • nanocrystalline graphite • plasma-enhanced chemical vapor deposition

- [1] R. Shah, M. Roshan, V. Mittal, <https://www.altenergymag.com/article/2025/01/Sodium-Batteries-for-use-in-Grid-Storage-Systems-and-Electric-Vehicles/44327> (accessed: June 2025).
- [2] H. S. Hirsh, Y. Li, D. H. S. Tan, M. Zhang, E. Zhao, Y. S. Meng, *Adv. Energy Mater.* **2020**, *10*, 2001274.
- [3] P. Phogat, S. Dey, M. Wan, *Mater. Sci. Eng. B* **2025**, *312*, 117870.
- [4] H. Kim, *ACS Mater. Au* **2023**, *3*, 571.
- [5] A. Yao, S. M. Benson, W. C. Chueh, *Nat. Energy* **2025**, *10*, 404.
- [6] S. K. Saju, S. Chattopadhyay, J. Xu, S. Alhashim, A. Pramanik, P. M. Ajayan, *Cell Rep. Phys. Sci.* **2024**, *5*, 101851.
- [7] C. Wu, Y. Yang, Y. Zhang, H. Xu, X. He, X. Wu, S. Chou, *Chem. Sci.* **2024**, *15*, 6244.
- [8] S. Tan, H. Yang, Z. Zhang, X. Xu, Y. Xu, J. Zhou, X. Zhou, Z. Pan, X. Rao, Y. Gu, Z. Wang, Y. Wu, X. Liu, Y. Zhang, *Molecules* **2023**, *28*, 3134.
- [9] J. Wang, L. Xi, C. Peng, X. Song, X. Wan, L. Sun, M. Liu, J. Liu, *Adv. Eng. Mater.* **2024**, *26*, 2302063.
- [10] W. Deng, H. Yang, H. Huo, Y. Yu, *Adv. Funct. Mater.* **2025**, *35*, 2504168.
- [11] C. M. Ghimbeu, A. Beda, B. Rétty, H. E. Marouazi, A. Vizintin, B. Tratnik, L. Simonin, J. Michel, J. Abou-Rjeily, R. Dominko, *Adv. Energy Mater.* **2024**, *14*, 2303833.
- [12] X. Wang, J. Dong, J. Ren, D. Nan, N. Huang, J. Li, J. Liu, *J. Electroanal. Chem.* **2025**, *988*, 119152.
- [13] J. Wang, J. Fan, X. Yue, M. Fan, Z. Xie, Z. Yang, J. Zhang, A. Abudula, G. Guan, *Chem. Eng. J.* **2025**, *511*, 161953.
- [14] A. Beda, C. Vaulot, F. Rabuel, M. Morcrette, C. M. Ghimbeu, *Energy Adv.* **2022**, *1*, 185.
- [15] L. Xiao, H. Lu, Y. Fang, M. L. Sushko, Y. Cao, X. Ai, H. Yang, J. Liu, *Adv. Energy Mater.* **2018**, *8*, 1703238.
- [16] M. Song, Z. Yi, R. Xu, J. Chen, J. Cheng, Z. Wang, Q. Liu, Q. Guo, L. Xie, C. Chen, *Energy Storage Mater.* **2022**, *51*, 620.
- [17] A. Beda, J. M. L. Meins, P. L. Taberna, P. Simon, C. M. Ghimbeu, *Sustainable Mater. Technol.* **2020**, *26*, e00227.
- [18] H.-G. Wang, W. Li, D.-P. Liu, X.-L. Feng, J. Wang, X.-Y. Yang, X. Zhang, Y. Zhu, Y. Zhang, *Adv. Mater.* **2017**, *29*, 1703012.
- [19] D. Idamayanti, A. Rochliadi, M. Iqbal, Z. Noer, R. Febrian, N. L. W. Septiani, B. S. Purwasasmita, B. Yuliarto, A. Nuruddin, *J. Energy Storage* **2024**, *89*, 111491.
- [20] X. Gao, Y. An, W. Zhang, M. Yu, L. Ci, J. Feng, *Mater. Technol.* **2018**, *33*, 810.
- [21] H. Guo, X. Qu, B. Xing, H. Zeng, W. Kang, S. Cheng, Y. Xing, J. He, C. Zhang, *Appl. Surf. Sci.* **2024**, *660*, 159999.
- [22] H. R. Sarma, J. Sun, Y. Hora, M. Forsyth, N. Byrne, *ChemElectroChem* **2023**, *10*, e202300127.
- [23] Y. Gao, Z. Hou, M. Jiang, D. Lei, X. Zhang, Y. Zhang, J. G. Wang, *J. Electroanal. Chem.* **2023**, *941*, 117525.
- [24] A. Beda, C. Villevieille, P.-L. Taberna, P. Simon, C. M. Ghimbeu, *J. Mater. Chem. A* **2020**, *8*, 5558.

- [25] X. X. He, J. H. Zhao, W. H. Lai, R. Li, Z. Yang, C. M. Xu, Y. Dai, Y. Gao, X. H. Liu, L. Li, G. Xu, Y. Qiao, S. L. Chou, M. Wu, *ACS Appl. Mater. Interfaces* **2021**, *13*, 44358.
- [26] B. Karaman, H. Tonnoir, D. Huo, B. Carré, A. F. Léonard, J. C. Gutiérrez, M. L. Piedboeuf, A. Celzard, V. Fierro, C. Davoisne, R. Janot, N. Job, *Carbon N. Y.* **2024**, 225, 119077.
- [27] Y. Pan, B. Ji, L. Wang, Y. Sun, L. Li, X. Wu, P. Zhou, *Electrochim. Acta* **2024**, 506, 145042.
- [28] L. Hu, G. Cheng, J. Ren, F. Wang, J. Ren, *Int. J. Electrochem. Sci.* **2019**, *14*, 2804.
- [29] L. Larbi, R. Wernert, P. Fioux, L. Croguennec, L. Monconduit, C. M. Ghimbeu, *ACS Appl. Mater. Interfaces* **2023**, *15*, 18992.
- [30] W. Deng, Y. Wang, Z. Chen, H. Huang, C. Chen, B. Pan, Y. Yang, S. He, H. Pan, H. Yang, Y. Yu, *Adv. Funct. Mater.* **2025**, 2501721.
- [31] O.-G. Simionescu, R. C. Popa, A. Avram, G. Dinescu, *Plasma Process. Polym.* **2020**, *17*, 1900246.
- [32] M. Gartner, M. Anastasescu, H. Stroescu, J. M. Calderon-Moreno, S. Preda, O.-G. Simionescu, A. Avram, O. Buiu, *Coatings* **2022**, *12*, 1274.
- [33] P. Scherrer, *Nach Ges Wiss Göttingen* **1918**, *2*, 8.
- [34] A. Sadezky, H. Muckenhuber, H. Grothe, R. Niessner, U. Pöschl, *Carbon N. Y.* **2005**, *43*, 1731.
- [35] A. Beda, S. Zallouz, S. Hajjar-Garreau, H. E. Marouazi, L. Simonin, C. M. Ghimbeu, *ACS Appl. Mater. Interfaces* **2024**, *16*, 68664.
- [36] N. Sun, Z. Guan, Y. Liu, Y. Cao, Q. Zhu, H. Liu, Z. Wang, P. Zhang, B. Xu, *Adv. Energy Mater.* **2019**, *9*, 1.
- [37] A. C. Ferrari, J. Robertson, *Phys. Rev. B* **2000**, *61*, 14095.
- [38] A. C. Ferrari, *Solid State Commun.* **2007**, *143*, 47.
- [39] I. Childres, L. Jauregui, W. Park, H. Caoa, Y. P. Chena, *New Dev. Photo Mater. Res.* **2013**, *1*, 1.
- [40] M. Wall, *Thermo Sci.* **2011**, *5*, 1.
- [41] A. C. Ferrari, J. Robertson, *Phys. Rev. B* **2001**, *63*, 121405(R).
- [42] C. Hu, S. Sedghi, A. Silvestre-Albero, G. G. Andersson, A. Sharma, P. Pendleton, F. Rodríguez-Reinoso, K. Kaneko, M. J. Biggs, *Carbon N. Y.* **2015**, *85*, 147.
- [43] X. Chen, N. Sawut, K. Chen, H. Li, J. Zhang, Z. Wang, M. Yang, G. Tang, X. Ai, H. Yang, Y. Fang, Y. Cao, *Energy Environ. Sci.* **2023**, *16*, 4041.
- [44] C. M. Ghimbeu, A. Beda, C. Vaulot, *Carbon N. Y.* **2025**, *240*, 120331.
- [45] H. Barua, A. Povitsky, *Math. Comput. Appl.* **2023**, *28*, 112.
- [46] R. He, T. D. Day, J. R. Sparks, N. F. Sullivan, J. V. Badding, *Adv. Mater.* **2016**, *28*, 5939.
- [47] S. Wild, C. Mahr, A. Rosenauer, T. Risse, S. Vasenkov, M. Bäumer, *Catal. Lett.* **2023**, *153*, 3405.
- [48] Z. Tang, R. Zhang, H. Wang, S. Zhou, Z. Pan, Y. Huang, D. Sun, Y. Tang, X. Ji, K. Amine, M. Shao, *Nat. Commun.* **2023**, *14*, 6024.
- [49] C. Qiu, A. Li, D. Qiu, Y. Wu, Z. Jiang, J. Zhang, J. Xiao, R. Yuan, Z. Jiang, X. Liu, X. Chen, H. Song, *ACS Nano* **2024**, *18*, 11941.
- [50] T. Zhao, L. Yan, L. Song, A. Li, Y. Xiong, Y. Tian, Z. Xiao, Y. Kuang, *J. Energy Storage* **2024**, *102*, 114209.
- [51] C. Bommier, X. Ji, *Small* **2018**, *14*, 1703576.
- [52] Y. Cao, L. Xiao, M. L. Sushko, W. Wang, B. Schwenzler, J. Xiao, Z. Nie, L. V. Saraf, Z. Yang, J. Liu, *Nano Lett.* **2012**, *12*, 3783.
- [53] B. Zhang, C. M. Ghimbeu, C. Laberty, C. Vix-Guterl, J.-M. Tarascon, *Adv. Energy Mater.* **2016**, *6*, 1501588.
- [54] S. Qiu, L. Xiao, M. L. Sushko, K. S. Han, Y. Shao, M. Yan, X. Liang, L. Mai, J. Feng, Y. Cao, X. Ai, H. Yang, J. Liu, *Adv. Energy Mater.* **2017**, *7*, 1700403.
- [55] Y. Morikawa, S. Nishimura, R. Hashimoto, M. Ohnuma, A. Yamada, *Adv. Energy Mater.* **2020**, *10*, 1903176.
- [56] C. M. Ghimbeu, J. Górká, V. Simone, L. Simonin, S. Martinet, C. Vix-Guterl, *Nano Energy* **2018**, *44*, 327.
- [57] P. Bai, Y. He, P. Xiong, X. Zhao, K. Xu, Y. Xu, *Energy Storage Mater.* **2018**, *13*, 274.
- [58] M. S. Lim, G. H. Lim, Y. J. Shin, J. S. Chae, J. W. Lee, R. K. Chul, *Energy Mater.* **2025**, *5*, 500104.
- [59] K. Wang, Y. Jin, S. Sun, Y. Huang, J. Peng, J. Luo, Q. Zhang, Y. Qiu, C. Fang, J. Han, *ACS Omega* **2017**, *2*, 1687.

Manuscript received: June 27, 2025

Revised manuscript received: September 5, 2025

Version of record online:
